IOP Publishing Plasma Physics and Controlled Fusion
Plasma Phys. Control. Fusion **62** (2020) 114001 (10pp) https://doi.org/10.1088/1361-6587/abb5e3

# Laser-driven proton acceleration via excitation of surface plasmon polaritons into $TiO_2$ nanotube array targets

**G Cristoforetti[1], F Baffigi[1], F Brandi[1], G D'Arrigo[2], A Fazzi[3,4], L Fulgentini[1], D Giove[4], P Koester[1], L Labate[1,5], G Maero[4,6], D Palla[1], M Romé[4,6], R Russo[2], D Terzani[1], P Tomassini[1] and L A Gizzi[1,5]**

[1] ILIL, Istituto Nazionale di Ottica, CNR, Pisa, Italy
[2] Istituto per la Microelettronica e Microsistemi, CNR, Catania, Italy
[3] Dipartimento di Energia, Politecnico di Milano, Milano, Italy
[4] INFN, Sez. Milano, Italy
[5] INFN, Sez. Pisa, Italy
[6] Dipartimento di Fisica, Università degli Studi di Milano, Milano, Italy

E-mail: gabriele.cristoforetti@cnr.it

Received 1 July 2020, revised 1 September 2020
Accepted for publication 7 September 2020
Published 2 October 2020

**Abstract**

In this paper we report the measurement of laser-driven proton acceleration obtained by irradiating nanotube array targets with ultrashort laser pulses at an intensity in excess of $10^{20}$ W cm$^{-2}$. The energetic spectra of forward accelerated protons show a larger flux and a higher proton cutoff energy if compared to flat foils of comparable thickness. Particle-In-Cell 2D simulations reveal that packed nanotube targets favour a better laser-plasma coupling and produce an efficient generation of fast electrons moving through the target. Due to their sub-wavelength size, the propagation of e.m. field into the tubes is made possible by the excitation of Surface Plasmon Polaritons, travelling down to the end of the target and assuring a continuous electron acceleration. The higher amount and energy of these electrons result in turn in a stronger electric sheath field on the rear surface of the target and in a more efficient acceleration of the protons via the target normal sheath acceleration mechanism.

Keywords: relativistic laser plasma interaction, high-fields plasmonics, ion acceleration, nanostructured targets

(Some figures may appear in colour only in the online journal)

## 1. Introduction

Laser-driven ion acceleration is nowadays an attractive and prolific research field for its potentiality to realize compact sources of energetic proton or light ion bunches. Target normal sheath acceleration (TNSA) [1] is currently raising a widespread interest, due to the simplicity of the mechanism, to its robustness, to the potential implementation at high rep-rate operation and also to its ability to produce laminar, collimated and high brightness short ion pulses [2–6].

In the typical experimental setup, the acceleration of protons/light ions is obtained by irradiating a thin solid foil - usually a few microns thick - with a relativistic sub-ps laser pulse. In a simplified description of the acceleration mechanism, relativistic suprathermal electrons (fast electrons) generated by laser-plasma interaction cross the bulk target and escape from its rear surface [7], producing a sheath electric field [8]. Such extremely intense field, reaching several $TV\ m^{-1}$, is normal to the rear surface and accelerates nearby ions in the forward direction, including the protons usually present

 

in the form of contaminants. Most of the current studies deal with the understanding of the key parameters in the process, in order to control the source, i.e. increase the monochromaticity of the ions, usually distributed in a broad energy spectrum, reduce the divergence of the beam and enhance the energy spectrum cutoff/charge. According to the scheme depicted above, the production of high-energy ions is related to the effectiveness of the electron acceleration on the front target surface. By using a simplified static model, where the acceleration of light ions does not affect the sheath field $E_s$ and they can be treated as test particles, it is found that $E_s$ depends both on the number density $n_h$ and on the the temperature $T_h$ of the fast electrons [9] reaching the rear surface, where $E_s \propto \sqrt{T_h n_h}$. It is therefore expected that higher cutoff energies and fluxes of light ions are produced for target geometries or interaction conditions able to improve the number and/or the temperature of the generated fast electrons.

In recent years, relativistic interaction of ultrashort laser pulses with nano- or micro-structured targets raised a considerable interest, mainly because of the large efficiency of laser absorption, which in some cases can reach values higher than 90% [10]. The enhancement of laser absorption is due to the volumetric heating of the structured material, where the laser can penetrate into the target for several micrometers [11], compared to an absorption length of the order of the collisional skin depth (usually a few tens of nanometers) in case of flat target irradiation [12]. Depending on the target geometry, the improved laser-target coupling can result in the heating of the plasma up to extreme temperatures, in a more efficient x-ray emission [13] or in the efficient acceleration and guiding of fast electrons [14–18]. It was shown that for particular target geometries (e.g. aligned array of nanotubes) the interaction can produce the efficient propagation of Mega-Ampere currents of relativistic electrons into the target, in turn resulting in the self-generation of a multi Mega-Gauss magnetic field on its rear surface [19]. A detailed inspection of the interaction process, by means of analytical approaches or kinetic Particle-in-cell (PIC) simulations, suggests that the boost of energetic electrons is related to the enhancement of electrostatic fields in proximity of the nanostructures[15] or to the generation of propagating e.m. waves [20] along their surfaces. Such phenomena can be related to the analogous enhancement of electrostatic field due to a localized Surface Plasmon Resonance (SPR) and to the excitation of propagating Surface Plasmon Polaritons (SPP), respectively, investigated in solid state plasmonics [21]. SPP are e.m. waves spatially confined near a dielectric-metal interface, where an abrupt jump of the dielectric function $\varepsilon$ from a positive to a negative value exists. They can be excited by light irradiation of the interface with suitable experimental setups and they can propagate for considerable distances. SPP waves reduce to electrostatic localized SPR for high wavevector values ($k_{SPP} = \frac{2\pi}{\lambda_{SPP}} \gg k_0 = \frac{2\pi}{\lambda_0}$) and to Sommerfeld-Zenneck waves [22, 23], i.e. grazing confined light waves, when $k_{SPP} \approx k_0$. The high confinement of the SPP fields, due to their evanescent character both into the dielectric and the metal media, and the ability of propagation for long distances with a low damping, motivates interest in the scientific community because of the potentiality to build plasmonic waveguides of dimensions beyond the diffraction limit, able to transport information at the speed of light. Such all-optical waveguides could overcome the limits of classical photonics allowing the construction of circuitry components with size typical of classical electronics, but with a much higher velocity.

In the relativistic irradiation regime [24], the solid target is ionized in a time comparable to an optical cycle and the field propagation into the produced plasma is ruled by the dielectric function

$$\epsilon = 1 - \frac{\omega_p^2}{\gamma\omega_0^2} \tag{1}$$

where $\omega_p$ is the plasma frequency and the $\gamma$ factor accounts for the electron inertia in the relativistic regime. This is equivalent to defining a relativistic mass $m_{rel} = m_e\gamma$ in the plasma frequency. In plasmas produced by laser irradiation of solid targets typically $\omega_p \gg \omega_0$ and the dielectric function is thus much less than 0, which prevents the laser light to penetrate beyond a thin layer of the order of a few nanometers. It is evident that equation (1) reduces to that expressing the dielectric function of a metal according to the Drude model, where $\gamma = 1$ (non-relativistic regime) and $\omega_p$ now accounts only for the valence electrons in the metal. This suggests that it is possible to extend the solid-state plasmonics to the high-fields irradiation regime, provided that non linear relativistic effects of electron dynamics are accounted for [24].

In solid-state plasmonics, the excitation of SPP is hampered by the requirements for the phase matching between SPP and laser light waves, since $k_{SPP} > k_0$. In case of irradiation on a flat dielectric-metal interface, the issue is usually overcome by means of appropriate coupling setups [21], i.e. by using a prism in the Otto [25] or in the Kretschmann [26] configuration. The utilization of nanostructured surfaces, however, can simplify the issue of momentum compensation and enable an easier excitation of SPP. A well-known approach is for example the grating assisted coupling, where the metal surface is patterned with a grating of grooves with an appropriate periodicity, so that the phase matching becomes possible for appropriate angles of incidence of the laser light. This scheme has been recently replicated in the high-fields regime, by demonstrating that SPP can be efficiently driven by a relativistic laser pulse impinging over a grating target at proper angles; experimental measurements showed that such configuration results in the generation of fast electron bunches, accelerated by the SPP field, emitted along the target surface [27].

Another classical approach for exciting SPP is that of using nanowire or nanotube arrays; in this case, the issue of phase matching is circumvented by irradiating the tips of the wires or of the tubes, where a structural symmetry breaking exists [28]. It is straightforward to extrapolate the same approach in the high-field regime, by irradiating nanowire/nanotube array targets with a relativistic laser pulse; this scheme is expected to result in the excitation of SPP and could explain

the Mega-Ampere currents of hot electrons measured in similar experiments [19]. In agreement with this picture, PIC simulations recently carried out by Andreev *et al* [20] confirmed that relativistic laser interaction with nanowire targets results in the formation of e.m. surface waves, joined with the generation of relativistic electrons, travelling at the light speed along the wire surface. Besides, detailed PIC simulations by Zou *et al* [29–31] depicted the excitation of propagating e.m. fields obtained by irradiating microchannel targets with relativistic laser pulses; the spatial distribution of the fields into the channels resembled typical TM eigenmodes in a waveguide, which is in agreement with the expected distribution of e.m. fields of an SPP. Zou *et al* [29–31] also showed the capability of these e.m. waves to accelerate relativistic electrons and, in turn, to efficiently accelerate protons from a CH foil located at the end of the microchannel array.

In the present work, we aim at investigating the capability of nanotube targets to accelerate protons via the TNSA mechanism. In the experiment a $TiO_2$ nanotube array of length 14 $\mu$m was irradiated by an ultrashort relativistic laser pulse at intensities in excess of $10^{20}$ W cm$^{-2}$. Laser-target interaction was monitored via optical spectroscopy of light scattered in the specular direction and proton acceleration on the rear surface of the nanotubes was investigated by means of a Thomson Parabola and a Time Of Flight detector. The mechanisms leading to the higher proton flux and energy cutoff compared to those obtained for Titanium foils of a comparable thickness, is discussed in view of 2D PIC simulations, showing the formation of SPP waves travelling along the nanowires/nanotube walls. Such SPPs give rise to an effective acceleration of relativistic electrons and in a higher electric sheath field on the rear of the target. Moreover, simulations also reveal the presence of two energy components in the proton spectrum, with the higher energy component progressively shifting to higher energy for a larger nanotube gaps, a clear signature of the SPP origin of this component. In contrast, the low energy component has a flat target-like behaviour dependent on the fill-factor of the target, as expected for acceleration driven by fast electrons propagating in the solid between channels.

## 2. Experimental setup

The measurements were carried out at the Intense Laser Irradiation Laboratory at INO-CNR (Pisa, Italy) using the Ti:Sa laser system delivering 3 J of energy on the target [32]. The laser pulse ($\lambda = 800$ nm, $\tau = 30$ fs) was focussed by means of an f/#4.5 Off-Axis-Parabola (OAP) in a spot of $\sim 3\times5$ $\mu$m$^2$ (FWHM), impinging on the target surface at an angle of incidence of 15°. Considering a Strehl ratio of 0.54, i.e. an energy of $\approx 1.6$ J enclosed into the laser spot, the laser intensity was $\approx 2.8\cdot10^{20}$ W cm$^{-2}$ ($a_0\approx 11$). The target consisted of a 14 $\mu$m-thick $TiO_2$ layer formed by an array of nanotubes, open on both ends, as shown in figure 1. The internal diameter of the nanotubes is $\sim$ 100–150 nm and two adjacent channels are separated by a wall of $\sim$ 50–80 nm.

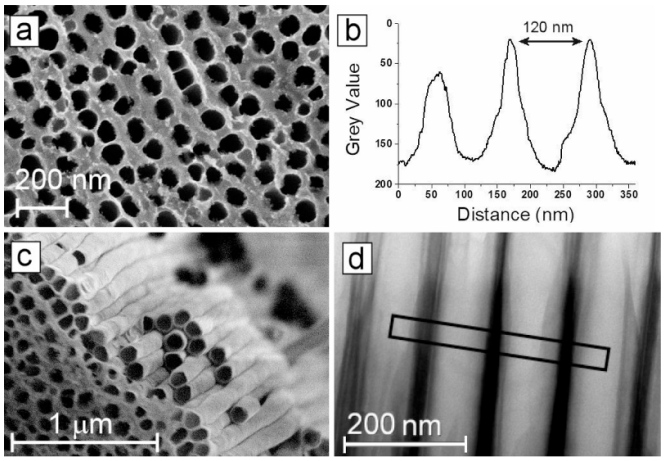


**Figure 1.** SEM images of a $TiO_2$ nanotube array target. Image (b) is the gray value profile obtained in the selected area highlighted in image (d), showing the side view of the target.

Concerning the preparation of the nanotube targets, Titanium foils approximately 14 $\mu$m-thick were used as anode in an electrochemical cell and were subject to potentiostatic anodization in a two-electrode system at room temperature. The cell was connected to a dc power supply using a platinum ring as a counter electrode. Considering the strong mechanical modification induced by electrochemical anodization during the transformation from metal Ti to Titanium Oxide nanopores array [33, 34], prior to anodization all samples were sandwiched in a glass epoxy double frame, cleaned with ethanol and dried. The electrolyte used to obtain long nanotube arrays, consisted of 0.25-0.5 wt% $NH_4F$ (98% ACS reagent) and ethylene glycol (99.8% anhydrous) solution with water concentrations of 1–3%. The final Ti oxide pores dimension was tuned by fixing the Ammonium fluoride concentration. A fixed voltage of 60 V, for about 1 h, was used for the processing; the cell current was monitored and the anodization process was stopped when the current was reduced by 2 orders of magnitude.

The performance of nanotube arrays in the laser-driven acceleration of protons was compared with that of pure Titanium foils of 12.5 $\mu$m thickness, which have a similar thickness of the substrate of the nanotube target. During the measurements, the targets were placed into a rigid holder with a perforated mask, in order to assure the planarity of the foils and the stability of the interaction point relative to the laser beam waist.

Ion acceleration was investigated by using a Thomson Parabola (TP) and a Time-Of-Flight (TOF) Silicon Carbide (SiC) fast diode. TP and TOF were placed on the rear side at 60 cm from the target, aligned on the normal direction to the surface and on a slightly tilted direction ($\sim 4$°), respectively. The two diagnostics were used simultaneously so that a cross-check of the measurements could be done. An additional TOF diamond thick detector, looking at the rear side at $\sim 6$° from the normal and 60 cm from the target, was used to investigate hot electrons escaping the target. The Thomson Parabola was housed

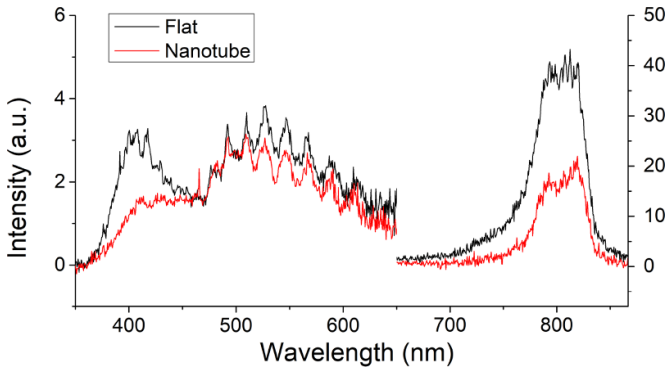


**Figure 2.** UV–Vis spectrum of plasma emission acquired during the interaction with flat and nanotube targets. The curves at wavelengths before and after 650 nm refer to left and right vertical axes, respectively, for sake of clarity.

in a separate vacuum chamber, operating at a pressure of $10^{-6}$ Torr, and differentially pumped with respect to the main target chamber. Ions are deflected by parallel electric and magnetic fields, depending on their energy, forming different parabolic traces according to their charge-to-mass ratios. Ions are finally detected through a multichannel plate (MCP) coupled to a phosphor screen, imaged by an Andor CCD camera. A detailed description of a Thomson Parabola working principle can be found in reference [35].

The trace of the TOF SiC diode, measured by a 500MHz digital oscilloscope (Wavesurfer 3054 LeCroy), showed clearly two well separated peaks, the first produced by the impact of X-rays and relativistic fast electrons and the second by energetic ions. Taking into account the TOF distance from the target, the time delay of the two detected peaks allows the measurement of the ion energy. A description and a discussion of the TOF measurements can be found in reference [32].

The TOF signal is converted in the number of particles impinging on the detector through Monte Carlo based simulations of the interaction between particles and the detector itself. The uncertainty of the measurements, dominated by the stochastic nature of the energy deposited into the detector (energy straggling), is less than 5%.

## 3. Interaction conditions

In this section we discuss the laser-target interaction conditions of the 'real' temporal profile of the Chirped Pulse Amplification (CPA) laser system which usually includes radiation reaching the target before the laser peak. It is therefore important to assess the effect of any precursor laser radiation on the integrity of the nanostructures. Indeed, the presence of any precursor radiation may generate a plasma, usually referred to as a 'pre-plasma', before the main peak reaches the target. This pre-plasma is expected to affect the laser-plasma interaction and the generation of fast electrons. It is therefore important to quantify the extension and the scalelength of such pre-plasma in our experiment.

In CPA laser systems, the intensity of the precursor radiation is usually quantified by the temporal contrast parameter, defined as the ratio of the peak intensity to the pedestal intensity, taken at a given time relative to the peak intensity. Cross-correlation measurements show that the nanosecond scale contrast due to Amplified Spontaneous Emission (ASE) in our system is better than $10^9$, while the contrast of the picosecond pedestal taken 10 ps before the peak is better than $\sim 10^7$ [36]. Moreover, dedicated shadowgraphic images of pre-plasma formation in a gas-jet showed that in our system the ASE emission focuses several hundred microns beyond the position of the waist of the main CPA pulse. This effect is due to the different divergence of ASE compared to that of the main CPA pulse, as previously discussed by Keppler *et al* [37]. By considering the ASE power contrast and the different focal positions, we finally estimate that the ASE intensity on the target surface is around $10^9$ W cm$^{-2}$. This value is too low to produce any significant pre-plasma able to strongly modify the interaction conditions of the main peak. Measurements performed with Ti targets of different thickness, showing an effective proton acceleration down to values of 2 microns, confirm the negligible effect of ASE in our laser facility. In the presence of a strong ASE, in fact, an abrupt fall of the proton acceleration occurs, in particular for thin targets, due to the disruption of the rear side produced by the induced shock wave. According to hydrodynamic simulations carried out with the 2D Eulerian code POLLUX, we estimated that the time needed by the shock wave induced by the ASE to reach the rear surface of a 12 microns target is around 2 ns, decreasing to less than 1 ns for targets of 2-3 microns. These values are significantly shorter than the ASE duration (4 ns), suggesting again that ASE does not play a significant role in our case. Conversely, the ps pedestal can reach an intensity on target of $\sim 10^{13}$ W cm$^{-2}$ and has a more relevant impact. To assess the role of the ps pedestal on the pre-plasma formation, we carried out additional 2D simulations with a flat Ti target by using the hydrodynamic Eulerian code POLLUX [38]. Similarly to the results reported elsewhere [39], our hydrodynamic simulations reveal a density profile of the pre-plasma characterized by different scalelength values at different densities. In the underdense region at densities lower than $\approx 0.3\ n_c$, the scalelength is of the order of 1 $\mu$m, while the profile becomes steeper at densities approaching the critical density and above, with scalelength values of $\sim 250$ nm and $\sim 150$ nm at $n_c$ and $3n_c$, respectively.

Additional information about the density profile of the pre-plasma can be experimentally obtained by means of UV-Visible spectroscopy of scattered light. In the present experiment we acquired spectra of the light scattered in the specular direction of the laser incidence. As shown in figure 2, beside the laser peak, both flat and nanotube target spectra reveal the presence of $2\omega_0$ ($\lambda = 400$ nm) and of $3/2\omega_0$ ($\lambda \approx 533$ nm) harmonics, which are signatures of laser-plasma coupling at critical and quarter-critical densities, respectively, as reported in detail in reference [40]. The three-halves harmonics, in particular, is produced by the non-linear coupling of the laser pulse with plasma waves driven by Two-Plasmon Decay instability

and needs a sufficiently smooth density profile to develop. As shown in reference [41, 42], in the case of ultrashort relativistic interaction, the minimum value of density scalelength at quarter-critical density to allow the onset of TPD instability is of the order of the laser wavelength, which can therefore be used as a diagnostics for inspecting the size of the pre-plasma.

As shown in figure 2, the $3/2\omega_0$ harmonics is well visible in the spectrum obtained with a flat foil. This suggests that the pre-plasma scalelength at $n_c/4$ is at least of the order of the laser wavelength, which is in agreement with the density profile retrieved by hydrodynamic simulations for flat foil interaction.

The $2\omega_0$ harmonics is also well visible in the spectrum, showing evidence of the laser interaction at the critical density. Due to relativistic transparency, the laser pulse is expected to propagate up to a region of even higher density, where the density profile is expected to be steeper.

In the case of $TiO_2$ nanotubes irradiation, the formation of a pre-plasma is even more important, since it could damage or destroy the nanostructures before the impact of the laser peak [43].

Due to the size of the nanotubes, smaller than the diffraction limit, it is unlikely that a large fraction of the laser pedestal can penetrate into the target, except a small percentage propagating via plasmonic effects in solid nanostructures (see below). So, a pre-plasma is expected to be produced mainly in the front surface of the target, rather than inside the holes. Therefore, the poor penetration of the laser pedestal into the tubes and the high ablation threshold of the insulator materials [44] suggest that the pre-plasma density into the holes at the arrival time of the main peak is in any case much lower than its relativistic critical density. Both the experimental results and the PIC simulations discussed later in the paper, corroborate this picture.

By comparing the optical spectra of flat foil and nanotubes, shown in figure 2, it is clear that $3/2\omega_0$ intensity is similar in the two cases, suggesting that the scalelength value of the pre-plasma in front of the target is comparable - and of the order of the micron - despite the different target geometry and composition.

The spectra also show that $\omega_0$ (laser) and $2\omega_0$ features are a factor 2 lower than in the flat foil spectrum. This result could be explained by the modulated plasma surface expected for a nanotube target, resulting in the scattering of laser and $2\omega_0$ harmonics in a wider angular range; the reduction of the two features by the same factor suggests however that the fraction of laser energy reaching the critical density is comparable for the two targets.

As a final remark we observe that the $3/2\omega_0$ peak is strongly modulated in both the flat and the nanotube spectra. The modulation corresponds to a frequency of 21 THz, which is comparable to $1/\tau_L$, where $\tau_L$ is the laser pulse duration. THz radiation of the same frequency has been often measured in ultrashort relativistic interaction, and could be due to the formation of transient currents in the underdense plasma [45, 46]. A discussion of this feature is however out of the scope of the present paper.

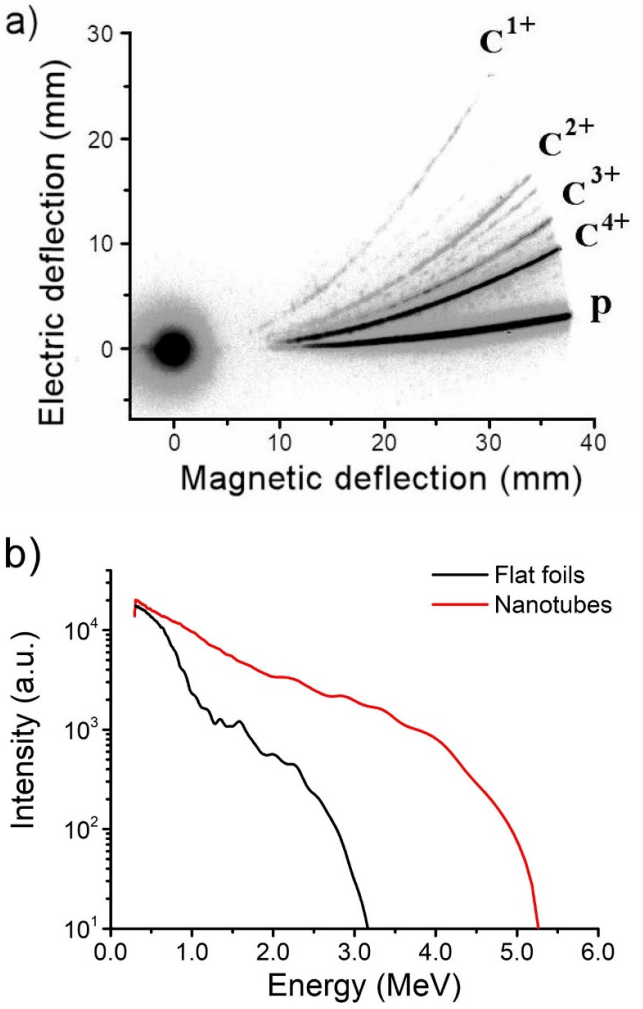


**Figure 3.** (a) raw image of the Thomson Parabola detector from a nanotube target; (b) single-shot proton spectra obtained with a flat Titanium foil (black line) and nanotube $TiO_2$ target (red line).

## 4. Experimental results

A typical raw image from the Thomson Parabola, obtained for a nanotube target, is shown in figure 3; along with the trace due the protons, other curves produced by heavier carbon and oxygen ions, having different charge-to-mass ratios, are well visible. The central bright spot, located at the origin of the parabolas, is produced by $\gamma$- and x-ray radiation moving straight through the electric and magnetic fields. As in most TNSA experiments, protons and carbon/oxygen ions here originate from hydrocarbon contaminants adsorbed on the rear surface of the target. Spectral calibration of the TP images was made possible after a detailed measurement of the electric and magnetic field distributions into the TP, including the edge effects of the permanent magnet, which allowed to calculate the ion deflection produced by the Lorentz force and finally to reconstruct the energy spectrum of the accelerated protons. Assuming that the brightness of the traces is correlated with the number of the ions [47], the measured traces allow to determine the proton cutoff energy and to estimate the ion flux.

Typical proton spectra obtained for Titanium foils and $TiO_2$ nanotube targets are also reported in figure 3. The figure shows that nanotubes provide a larger flux of protons and a higher cutoff energy. The cutoff value is here calculated by considering the signal exceeding 3 times the RMS of the noise on the detector. The cutoff energy obtained for the nanotube targets is in the range $(4.3-6.0)\pm0.2$ MeV, where the uncertainty is calculated by considering RMS noise on the detector. This value is in average $\approx 1.5$ times larger than the value obtained for the Ti foils, that was in the range $(3.3-4.0)\pm0.2$ MeV. An additional systematic uncertainty of $\sim 15\%$, due to the pinhole size and to the uncertainty in the electric and magnetic fields measurement, should be considered.

Time-Of-Flight measurements showed, as well, a similar enhancement of the energy cutoff for nanotube targets, as visible in figure 4. TOF traces show a good reproducibility shot by shot, as visible from the figure. Comparing the signals on the oscilloscope, it is evident that with nanotubes the protons reach the detector a few nanoseconds before than in the case of foil targets, and produce a signal which is $\approx 3$ times higher. Here, however, due to the lower sensitivity of the TOF detector and possibly also to a slightly out-of-normal angle of acquisition, the cutoff values for foils and nanotubes are $\approx 2.8$ MeV and $\approx 4.2$ MeV, respectively.

It is worth noticing that the thickness of the Ti foils is slightly smaller than that of the nanotube targets. However this small difference is not expected to significantly affect these results. We also exclude that the composition and the conductive properties of the target can play a significant role in the acceleration process. This is suggested by the plethora of targets of different composition which have been tested in a previous set of experiments, showing a substantial lack of material dependence [40].

The above arguments suggest that the different performance of Ti foils and $TiO_2$ nanotube targets in accelerating protons is due to the presence of the nanostructures, rather than to the target composition or thickness.

We also note that, considering the laser pulse duration, the energy delivered on the target and the thickness of the foil, the cutoff energies obtained for the standard foil target are in general agreement with previous results reported in literature and with the expected scaling [48].

Finally, it is worth noticing that TP and TOF measurements provide an evidence that the generation of fast electrons during laser plasma interaction is more efficient with nanotube targets than with flat foils. In TP raw images, this is suggested by the much more intense spot produced by $\gamma$- and x-ray radiation (comparison not shown here), in turn consisting of Bremsstrahlung emission of fast electrons after colliding with cold target ions. This is also confirmed by the intensity of the electron peak in the oscilloscope trace obtained with the thick diamond detector, as shown in figure 4(a).

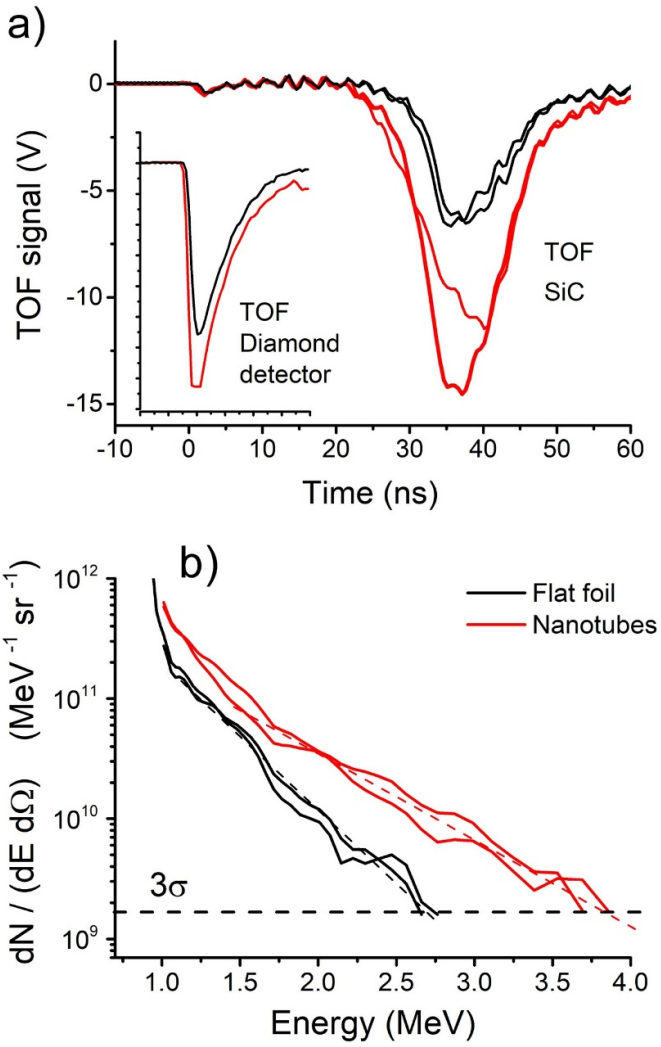


**Figure 4.** (a) TOF signals obtained by SiC fast diode and diamond detectors and (b) proton spectra obtained for flat foils and nanotube targets. Results from two different shots are reported for each target type for SiC detectors, to highlight the good reproducibility of the proton spectra. The time zero corresponds to the laser shot. The oblique dashed lines are exponential curves fitting the proton spectra. The horizontal dashed line is the $3\sigma$ noise level.

## 5. Particle-in-cell simulations

In order to understand the mechanisms leading to the effective proton acceleration observed with nanotube targets, PIC simulations were carried out with the Aladyn code [49] in 2D Cartesian geometry.

The p-polarized laser pulse, with Gaussian intensity profile in the transverse coordinate and focal spot FWHM $= 4\ \mu$m, enters the computational box from the left edge and impinges on the target at normal or at 15° incidence at time ct $\approx 13\ \mu$m, i.e. $\approx 43$ fs after the beginning of the simulation. The laser time profile was modelled by $I(t) = I_0 \cos^4(\pi t/2\tau)$ where $2\tau = 84$ fs corresponds to a pulse length at FWHM of 30 fs. The size of the numerical box was set to $L_x \cdot L_y = 80 \cdot 60\ \mu m^2$ and the grid cell to $dx \cdot dy = 12 \cdot 6\ nm^2$, assuring reasonable space-time resolution. The target consisted of pure Titanium in both nanotube and foil target simulations, with an initial $Ti^{2+}$ density set to $5.2 \cdot 10^{22}$ cm$^{-3}$, corresponding to a plasma electron density $n_e = 60\ n_c$, where $n_c$ is the critical plasma density for the laser wavelength. Due to the 2D character of the

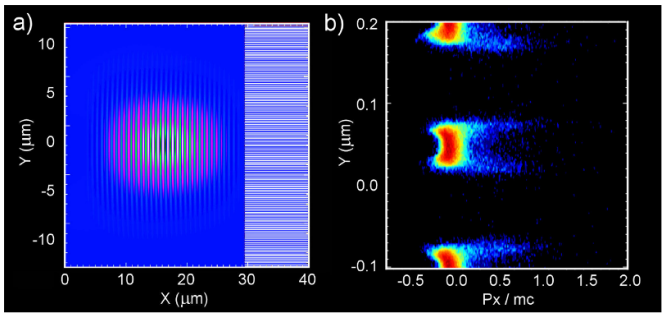


**Figure 5.** (a) simulation box and laser field at the beginning of the simulation ($ct = 0$ $\mu$m). (b) longitudinal momentum Px vs. y position into a nanotube target at time $ct = 10$ $\mu$m for the case of normal incidence of the laser and for a gap of 100 nm between the wires.

simulation, the nanotube target was modelled as a nanowire regular array, consisting of Ti wires of 50 nm diameter, separated by gaps of different size, as shown in figure 5(a). The extrapolation of the simulation results to a 3D nanotube structure will be discussed below. On the rear side of the target, a thin layer of hydrogen was placed behind the nanotube tips (corresponding to the rear surface for a flat foil) to allow for the generation of the proton beam. In the PIC code, 144 (macro)electrons and 324 (macro)protons per cell were used. During dynamical laser-plasma interaction, field ionization using the ADK model was activated. During the simulation, the ionization level of Ti ions rises from the initial Z = 2 to a final Z ≈ 18 in the nanotube walls.

The normalized energy distributions of the protons at the end of the simulation ($ct = 70$ $\mu$m), taken behind the target, are plotted in figure 6(c)-(d). Normal laser irradiation ($\theta = 0$) of the nanotubes results in a larger proton cutoff with respect to irradiation at larger angles (e.g. $\theta = 15^{\circ}$). Just for comparison, the proton spectrum obtained by irradiating a plain target at an angle $\theta = 15^{\circ}$ was also reported in the figure. In this case an exponential pre-plasma ramp with density scalelength of 150 nm was placed in front of the target to reproduce the expected interaction conditions. By comparing these spectral distributions with those reported in figures 3–4, a reasonable agreement of the proton cutoffs between simulations and the experimental data becomes evident.

The higher proton cutoff obtained for nanotube targets can be explained by the enhancement of the longitudinal electric field on the rear of the target, as shown in figure 7. This supports the idea that protons are accelerated by TNSA mechanism, even in case of nanostructured targets.

In the case of a nanotube target, the $E_x$ field, produced by the escape of the fast electrons from the target, reaches values of a few tens of TV/m, while it is only a few TV/m for a flat target. Simulations show that this longitudinal field results in the generation of a proton beam with a small angular divergence ($\Delta\varphi < 10°$), which is emitted normally to the rear surface, whatever is the angle of laser incidence on the front target surface.

Further simulations were carried out by including a homogeneous underdense pre-plasma $0.02 < n_e/n_c < 1$ into

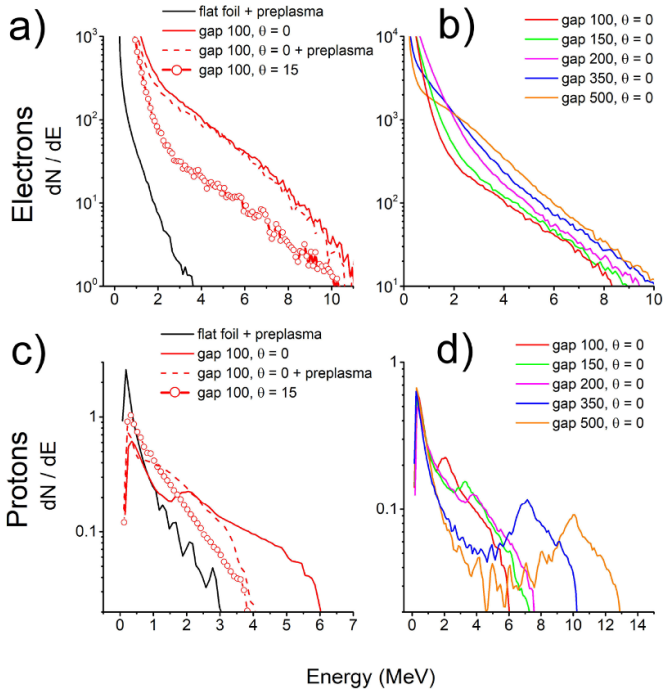


**Figure 6.** Spectra of fast electrons spatially integrated in the central region of the computational box at time $ct = 20$ $\mu$m ((a) and (b)) and normalized spectral distributions of accelerated protons ((c) and (d)) at time $ct = 70$ $\mu$m, obtained by PIC simulations. Images (a) and (c) compare the spectrum obtained for a flat target with those obtained for nanotube targets with 100 nm gap size, incidence angles $\theta = 0^{\circ}$ and $\theta = 15^{\circ}$ and in the case where gaps are filled by a pre-plasma with $n_e = 0.025$ $n_c$. Images (b) and (d) show the spectra obtained with nanotubes of different size and normal laser incidence.

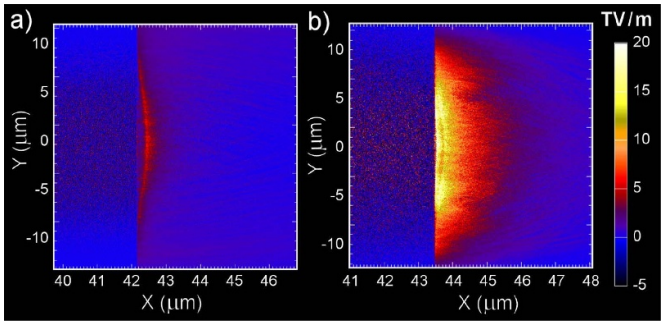


**Figure 7.** Longitudinal electric field behind the rear surface of the target at time $ct = 10$ $\mu$m for a) a flat target and b) a nanotube target with a gap = 100 nm between the wires.

the nanotube gaps to investigate the effect of the laser ps pedestal on the laser plasma coupling as shown in figure 6(c). With this simplified target model we aim at investigating the effect of the formation of a pre-plasma into the tubes as discussed above. The results show that the presence of a pre-plasma leads to a less effective proton acceleration with lower high-energy cutoffs (figure 6), due to a degradation of the laser-plasma coupling (see below).

A deeper insight into the acceleration of protons can be obtained by looking at the electromagnetic fields inside the target gaps. At early times, i.e. when the leading part of the

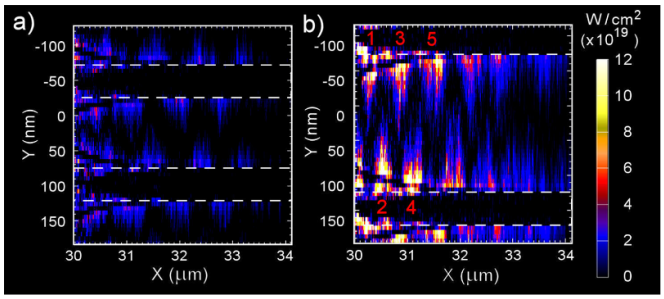


**Figure 8.** Longitudinal component of the Poynting vector (W m$^{-2}$) of the e.m. field for nanotube targets with a gap of 100 nm (a) and 200 nm (b) between the wires. The images refer to time $ct = 10$ *mu*m and for the case of normal incidence of the laser.

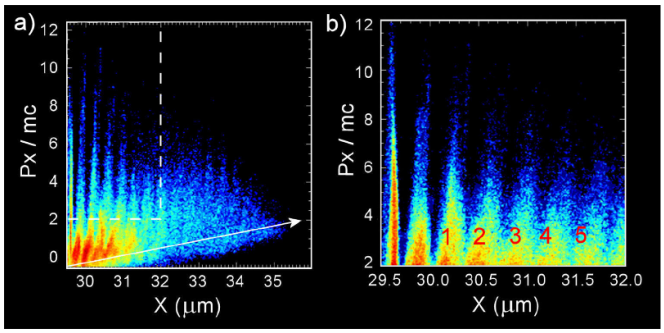


**Figure 9.** Longitudinal momentum Px of electrons vs. x position into a target channel with size of 200 nm and at time $ct = 10$ $\mu$m. Image (b) is a magnification of the dashed region in the plot on image (a).

laser pulse hits the front surface, the interaction gives rise to an oscillating e.m. field propagating into the gaps, i.e. along the edges of the nanotubes, where electric and magnetic fields oscillate in trasverse directions. This is clearly shown in figure 8, where the longitudinal component of the Poynting vector of the propagating e.m. field is plotted at time $ct = 10$ $\mu$m along the longitudinal extension of the nanotube in the front part of the target (nanotube tips are located at $x = 29.5$ $\mu$m). In phase with the e.m. field, an oscillating longitudinal electrostatic Ex field is also clearly visible along the nanotube edges. The trailing part of the laser pulse, at the opposite, is largely reflected by the plasma expanding at the tip of the nanotube, which rapidly fills the vacuum gap, as visible on the left side of figure 8(b). The e.m. field has the structure of a Surface Plasmon Polariton (SPP) wave excited at the interface between a metal and a dielectric, i.e. between media with a negative and a positive value of the dielectric function. Similarly, in the present case, the nanotube edge separates a subcritical (gap) and an overcritical (wall) plasma regions, with values of the dielectric function of opposite sign. As expected, the intensity of the e.m. field into the gap rapidly falls with increasing distance from the nanotube/gap interface, showing an evanescent behaviour. This results in a confinement of the wave close to the wall surface. By considering the continuity relation of $\varepsilon E_y$ at the vacuum-nanowire interface and the expression of the dielectric constant in the relativistic regime (equation 1), the transverse electric field $E_y$ into the overdense plasma is expected to be much lower than in the gap by a factor $\approx (1 - n_{e,+}/\gamma n_c)/(1 - n_{e,-}/\gamma n_c) \approx 50$ , where $n_{e,+}$ and $n_{e,-}$ are the electron densities in the wall and in the gap, respectively.

The spatial structure of the e.m. field of the SPP wave exhibits the typical asymmetric zig-zag distribution, which is usually produced by the interference of $TM_0$ and $TE_1$ modes [28]; a similar distribution has been experimentally observed in a solid state nanowire by imaging the luminescence of Quantum Dots covering the lateral surface [50]. The asymmetric transverse structure of the fields can also be driven by the coupling of the opposite evanescent fields into the gap.

Figure 8 shows that the wavevector of the surface e.m. wave is $k_{SPP} \sim k_0$, as expected for cases where $\omega_0 << \omega_p$, and the SPP acquires the features of a Sommerfeld-Zenneck wave [22, 23]. This makes easier the momentum matching with the laser light and therefore the excitation of the SPP at the nanotube tip, which is usually much more complex for higher frequency SPP waves. Simulations also show that the increase of the diameter of the nanotube leads to a better laser-SPP wave coupling, resulting in a higher energy transferred to the wave and finally in a higher proton cutoff; this can be seen by comparing the Poynting vector intensity of the SPP waves obtained for gaps of 100 nm and 200 nm, shown in figure 8. For a gap of 100 nm the Poynting vector of the SPP is only $\sim 9\%$ of that of the incident laser, but it rises to $\sim 30\%$ and $\sim 45\%$ for gap sizes of 200 nm and 500 nm. This leads to higher proton energy cutoffs when larger nanotubes are used, as shown in figure 6.

The inspection of the electron phase space $P_x$ vs. $y$ plot shown in figure 5(b) shows that the evanescent field into the gaps produces an electron acceleration along the nanotube length, which occurs mainly at the wall-gap interface. Electrons are accelerated by the $J \times B$ force as well as by the longitudinal electrostatic field. These electrons, initially extracted from the overdense region, gain energy from the SPP wave damping its propagation into the target. While the electrons into the channels move forward, those into the wires have a null or a small negative momentum, providing a return current neutralizing charge separation and enabling forward acceleration of 'hot' electrons.

A deeper understanding of the electron acceleration can be obtained by looking at the $P_x$ vs. $x$ plot of the electrons contained into the gap, shown in figure 9. Higher energy electrons, highlighted in figure 9(b) are spatially bunched at the positions of the strongest SPP e.m. fields, which is evident by comparing with figure 8(b) (corresponding peaks are numbered for the sake of clarity). These electrons are accelerated by the SPP fields to a velocity close to $c$ and therefore remains in phase with the wave and therefore bunched. Since the laser intensity that reaches the target surface and penetrates into the tubes increases with time, it is evident that the most energetic electrons are on the left of figure 9, where e.m. intensity is higher. The electrons with lower energy in figure 9, with a velocity significantly lower than $c$, are located in the right and at the bottom of the plot, and are accelerated in the early

part of the laser pulse, when the intensity is lower, or they are accelerated starting from positions not in phase with the SPP peak, respectively. In both cases, they are not bunched with the wave, but anyway they progressively gain energy by travelling into the channel, as highlighted by the white arrow in the figure.

The spectra of the fast electrons, which are forward moving ($P_x > 0$) into the nanotubes at time ct = 20 $\mu$m, are reported in figure 6 for the same cases discussed above. It is evident that the higher values of the proton cutoff are correlated with the cases of more efficient electron acceleration. In particular, figure 6 shows that the presence of a pre-plasma into the gaps results in a slightly less efficient electron acceleration, as discussed above. The slight difference between electron spectra with and without a pre-plasma, shown in figure 6, becomes more relevant at later simulation times, suggesting that the pre-plasma enhances the damping of the SPP, reducing their penetration. In case of pre-plasma, the amount of fast electrons with energy higher than 2 MeV is around 85% of that without the pre-plasma at time $ct = 20$ $\mu$m, but this value falls to 45% at time $ct = 30$ $\mu$m.

In figure 6, it is shown that the more intense SPP waves induced in gaps of increasing size result in a progressive larger number of fast electrons and, correspondingly, to higher cutoff energies for accelerated protons. The analysis of the proton spectra, in particular, reveals the presence of two energy components, which are convoluted and barely visible for nanotubes of smaller size, but tend to detach, becoming more evident, for nanotubes of larger size. The low energy component has an energy spectrum similar to that of protons accelerated in a flat target and, for analogy, is probably produced by fast electrons propagating into the nanotube walls (or into the nanowires). Simulations show that the intensity of this component falls for larger gap sizes (not visible in figure 6d since the spectra are here normalized), in agreement with the progressive reduction of the fill factor of the target for larger nanotubes. The high energy component moves to higher energies for larger values of the gap size, and is generated by the fast electrons accelerated into the tubes. Also this component becomes less intense for larger nanotubes, which is probably due to the progressive smaller amount of contaminant due to the lower fill factor. Such drawback could be however overcome by attaching a thin foil behind the nanotube array, as proposed by Zou *et al* [29–31]

The mechanisms depicted above are similar to those found by Zou *et al* [29–31], describing the relativistic irradiation of microchannels via 2D and 3D PIC simulations. In both cases, electron are accelerated by surfaces waves excited at the channel-vacuum interface. Differently from the works of Zou *et al* however, the size of the channels is here below the diffraction limit of the laser light, and approaches the range explored by Zou *et al* only at the largest size boundary. These circumstances make the above described phenomena fall in the more general framework of high-field plasmonics, not mentioned in the works of Zou *et al*.

An ad hoc discussion should be deserved to the extrapolation of the PIC simulations to the 3D geometry. As anticipated above, the target model used here and represented in figure 5(a) is the projection on the polarization plane of our real nanotube target. Moreover, the same model would also represent nanowire targets, which, in the real space, are significantly different from nanotubes and are expected to behave differently. For this reason, a simple extrapolation of the 2D kinetic results to our 3D geometry is an oversimplified step, which can lead to incorrect conclusions. The spatial structure and the propagation of SPP modes in nanotubes are in literature less explored than in nanowires. Moreover, finite-difference-time-domain simulations and experiments show a strong dependence of resonance SPR wavelength and SPP modes on the size and the thickness of the tube, and on the composition of the external medium in which nanotubes are embedded [51, 52]. It is shown that similarly to the case of nanowires, SPP waves with different azimuthal symmetry ($m = 0, \pm 1, \pm 2, ...$) can be excited on the dielectric-metal interface [51, 53, 54]. Such modes can be excited in the dielectric medium both into and outside the tube. In the present case, due to the array structure, only the former modes can be excited. We can therefore speculate that the SPP structure obtained in 2D PIC simulations indicate the formation of SPP modes into the tube, propagating along the edges of the overdense plasma. Such model has been successfully verified by using 3D PIC simulations by Zou *et al* [30], modelling relativistic irradiation of a micro-size channel by using a circularly polarized laser pulse. It seems therefore reasonable to extrapolate the validity of the model in 3D geometry also for linearly polarized pulses, although a systematic set of 3D PIC simulations is needed for quantitative and optimization purposes.

## 6. Conclusions

In summary, we showed that nanotube array targets can be used to enhance laser-driven proton acceleration via the TNSA technique. In the present experiment, the irradiation of a 14 $\mu$m thick $TiO_2$ nanotube disordered array by an ultrashort relativistic laser pulse at intensity in excess of $10^{20}$ W cm$^{-2}$ resulted in a more efficient proton acceleration than that obtained by using a flat Titanium target of comparable thickness, showing a higher flux and an enhancement of the cutoff energy by a factor $\sim 1.5$. PIC simulations suggest that the improved efficiency is related to the effective acceleration of fast electrons driven by the e.m. fields propagating into the nanotube gaps via the $J \times B$ force. Similarly to solid-state plasmonics, the propagation of e.m. fields into the nanotubes, with a sub-wavelength size, is made possible by the excitation of Surface Plasmon Polaritons at the interface between vacuum (hole) and overdense (nanotube wall) plasma. Despite being damped by the fast electron acceleration via the $J \times B$ force, SPP efficiently propagate at the speed of light up to the end of the tubes, assuring a continuous acceleration of the electrons along the channels. The sheath field produced by such electrons on the rear side of the target results in the acceleration of a high-energy proton population, determining an increase of the spectral cutoff. Simulations finally suggest that the performance of the TNSA can be further

improved by increasing the size of the holes and by enhancing the laser contrast.

## Acknowledgments

This project has received funding from the CNR funded Italian research Network ELI-Italy and from the L3IA INFN Experiment of CSN5. We gratefully acknowledge support from the Central Laser Facility for in kind contribution to the experimental set up described in this experiment.

## ORCID iDs

G Cristoforetti https://orcid.org/0000-0001-9420-9080
F Brandi https://orcid.org/0000-0003-2717-3748
A Fazzi https://orcid.org/0000-0001-5384-9962
M Romé https://orcid.org/0000-0003-3490-7949

## References

[1] Wilks S C *et al* 2001 *Phys. Plasmas* **8** 542
[2] Macchi A, Borghesi M and Passoni M 2013 *Rev. Mod. Phys.* **85** 751
[3] Daido H, Nishiuchi M and Pirozhkov A S 2012 *Rep. Prog. Phys.* **75** 056401
[4] Snavely R A *et al* 2000 *Phys. Rev. Lett.* **85** 2945–8
[5] Wagner F *et al* 2016 *Phys. Rev. Lett.* **116** 205002
[6] Poole P L *et al* 2018 *New J. Phys.* **20** 013019
[7] Gizzi L A *et al* 2007 *Plasma Phys. Control. Fusion* **49** B211
[8] Romagnani L *et al* 2008 *Laser Part. Beams* **26** 241
[9] Hatchett S P *et al* 2000 *Phys. Plasmas* **7** 2076
[10] Cao L, Gu Y, Zhao Z, Cao L, Huang W, Zhou W, He X T, Yu W and Yu M Y 2010 *Phys. Plasmas* **17** 043103
[11] Bargsten C *et al* 2017 *Sci. Adv.* **3** e1601558
[12] Purvis M A *et al* 2013 *Nat. Photonics* **7** 796
[13] Hollinger R *et al* 2017 *Optica* **4** 1344
[14] Cristoforetti G *et al* 2017 *Sci. Rep.* **7** 1479
[15] Sarkar D *et al* 2017 *APL Photonics* **2** 066105
[16] Moreau A *et al* 2020 *Plasma Phys. Control. Fusion* **16** 014014
[17] Khaghani D *et al* 2017 *Sci. Rep.* **7** 11366
[18] Jiang S *et al* 2016 *Phys. Rev. Lett.* **116** 085002
[19] Chatterjee G *et al* 2012 *Phys. Rev. Lett.* **108** 235005
[20] Andreev A *et al* 2016 *Plasma Phys. Control. Fusion* **58** 014038
[21] Maier S A 2007 *Plasmonics: Fundamentals and Applications* (Berlin: Springer)
[22] Zenneck J 1907 *Ann. Phys., Lpz.* **23** 846
[23] Sommerfeld A 1909 *Ann. Phys., Lpz.* **28** 665
[24] Macchi A 2018 *Phys. Plasmas* **25** 031906
[25] Otto A 1968 *Z. Phys.* **216** 398
[26] Kretschmann E and Raether H 1968 *Z. Naturforsch.* **23A** 2135
[27] Fedeli L *et al* 2016 *Phys. Rev. Lett.* **116** 015001
[28] Wei H, Pan D and Xu H 2015 *Nanoscale* **7** 19053
[29] Zou D, Pukhov A, Yi L, HB Zhuo T Y, Yin Y and Shao F 2017 *Sci. Rep.* **7** 42666
[30] Zou D, Yu D, Yu M, Huang T, Pukhov A, Zhuo H, Zhuo C and Ruan S 2019 *Nucl. Fusion* **59** 066034
[31] Zou D *et al* 2019 *Phys. Plasmas* **26** 123105
[32] Gizzi L A *et al* 2017 *Appl. Sci.* **7** 984
[33] Shankar K, Mor G K, Prakasam H E, Yoriya S, Paulose M, Varghese O K and Grimes C A 2007 *Nanotechnology* **18** 065707
[34] Li L L, Tsai C Y, Wu H P, Chenb C C and Diau E W G 2010 *J. Mater. Chem.* **20** 2753
[35] Harres K *et al* 2008 *Rev. Sci. Instrum.* **79** 093306
[36] Gizzi L *et al* 2018 *Nucl. Instrum. Methods Phys. Res.* A **909** 160
[37] Keppler S, Hornung M, Bodefeld R, Savert A, Liebetrau H, Hein J and Kaluza M C 2014 *Opt. Express* **22** 11228
[38] Pert G J 1989 *J. Plasma Phys.* **41** 263
[39] Kemp G E *et al* 2015 *Phys. Plasmas* **22** 013110
[40] Gizzi L A *et al* 2016 *Nucl. Instrum. Methods Phys. Res.* A **829** 144
[41] Veisz L, Theobald W, Feurer T, Schwoerer H, Uschmann I, Renner O and Sauerbrey R 2004 *Phys. Plasmas* **11** 3311
[42] Li C *et al* 2011 *Phys. Rev.* E **84** 036405
[43] Cristoforetti G *et al* 2014 *Plasma Phys. Control. Fusion* **56** 095001
[44] Stuart B, Feit M, Rubenchik A, Shore B and Perry M 1995 *Phys. Rev. Lett.* **74** 2248
[45] Liao G Q *et al* 2016 *Phys. Plasmas* **23** 013104
[46] Wu H C, Sheng Z M and Zhang J 2008 *Phys. Rev.* E **77** 046405
[47] Prasad R *et al* 2010 *Nucl. Instrum. Methods Phys. Res.* A **623** 712
[48] Fuchs J *et al* 2006 *Nat. Phys.* **2** 48
[49] Benedetti C, Sgattoni A, Turchetti G and Londrillo P 2008 *IEEE Trans. Plasma Sci.* **36** 1790
[50] Wei H, Pan D and Xu H 2011 *Nano Lett.* **11** 471
[51] Segui S, Gervasoni J L and Arista N R 2007 *Radiat. Phys. Chem.* **76** 582
[52] Kohl J, Fireman M and O'Carroll D M 2011 *Phys. Rev.* B **84** 235118
[53] Song J, Zaccaria R P, Dong G, Fabrizio E D, Yu M B and Lo G Q 2011 *Opt. Express* **19** 25206
[54] Ni H *et al* 2018 *Opt. Mater. Express* **8** 3676